We are IntechOpen, the world's leading publisher of Open Access books
Built by scientists, for scientists

6,900
Open access books available

186,000
International authors and editors

200M
Downloads

Our authors are among the

154
Countries delivered to

TOP 1%
most cited scientists

12.2%
Contributors from top 500 universities

CLARIVATE ANALYTICS

BOOK CITATION INDEX

INDEXED

WEB OF SCIENCE™

Selection of our books indexed in the Book Citation Index
in Web of Science™ Core Collection (BKCI)

Interested in publishing with us?
Contact book.department@intechopen.com

Numbers displayed above are based on latest data collected.
For more information visit www.intechopen.com

Optical Three-axis Tactile Sensor

Ohka, M.

Graduate School of Information Science, Nagoya University
Japan

1. Introduction

The three-axis tactile sensor has attracted the greatest anticipation for improving manipulation because a robot must detect the distribution not only of normal force but also of tangential force applied to its finger surfaces (Ohka, M. et al., 1994). Material and stability recognition capabilities are advantages of a robotic hand equipped with the three-axis tactile sensor (Takeuchi, S. et al., 1994). In peg-in-hole, a robot can compensate for its lack of degrees of freedom by optimum grasping force, allowing an object to move between two fingers using measured shearing force occurring on the finger surfaces (Brovac, B. at al., 1996). Also, a micro-robot would be required to remove any object attached to the inside a blood-vessel or pipe wall (Guo, S. et al., 1996; Mineta, T. et al., 2001; Yoshida, K. et al., 2002). It therefore becomes necessary to measure not only the normal force but also the shearing force.

Principle of the three-axis tactile sensor is described in this chapter. The authors have produced three kinds of three-axis tactile sensor: one columnar and four conical feelers type, none columnar feeler type for micro robots and a hemispherical type for humanoid robotic hands. Finally, a tactile information processing is presented to apply it to robotic object-recognition. The information processing method is based on a mathematical model formulated according to human tactile sensation.

2. Principle of Three-axis Tactile Sensor

2.1 Optical tactile sensor

Tactile sensors have been developed using measurements of strain produced in sensing materials that are detected using physical quantities such as electric resistance and capacity, magnetic intensity, voltage and light intensity (Nicholls, H. R., 1992). The optical tactile sensor shown in Fig. 1, which is one of these sensors, comprises an optical waveguide plate, which is made of transparent acrylic and is illuminated along its edge by a light source (Mott, D. H. et al., 1984; Tanie, K. et al., 1986; Nicholls, H. R., 1990; Maekawa, H. et al., 1992). The light directed into the plate remains within it due to the total internal reflection generated, since the plate is surrounded by air having a lower refractive index than the plate. A rubber sheet featuring an array of conical feelers is placed on the plate to keep the array surface in contact with the plate. If an object contacts the back of the rubber sheet, resulting in contact pressure, the feelers collapse, and at the points where these feelers collapse, light is diffusely reflected out of the reverse surface of the plate because the rubber has a higher refractive index than the plate. The distribution of contact pressure is calculated

from the bright areas viewed from the reverse surface of the plate.

The sensitivity of the optical tactile sensor can be adjusted by texture morphology and hardness of the sheet. The texture can be easily made fine with a mold suited for micro-machining because the texture is controlled by adjusting the process of pouring the rubber into the mold. This process enables the production of a micro-tactile sensor with high density and sensitivity by using the abovementioned principle of the optical tactile sensor. However, this method can detect only distributed pressure applied vertically to the sensing surface and needs a new idea to sense the shearing force. In this chapter, the original optical tactile sensor is called a uni-axial optical tactile sensor.

If we produce molds with complex structures to make rubber sheets comprising two types of feeler arrays attached to opposite sides of the rubber sheet, it will be possible to improve the uni-axial tactile sensor for use in three-axis tactile sensors (Ohka, M. et al., 1995, 1996, 2004). One of these types is a sparse array of columnar feelers that make contact with the object to be recognized; the other is a dense array of conical feelers that maintain contact with the waveguide plate. Because each columnar feeler is arranged on several conical feelers so that it presses against conical feelers under the action of an applied force, three components of the force vector are identified by distribution of the conical feelers' contact-areas.

Besides of the abovementioned three-axis tactile sensor comprised of two kinds of feelers, there is another design for ease of miniaturization. In the three-axis tactile sensor, the optical uni-axial tactile sensor is adopted as the sensor hardware and three-axis force is determined by image data processing of conical feeler's contact-areas to detect three-axis force (Ohka, M. et al., 1999, 2005a). In the algorithm, an array of conical feelers is adopted as the texture of the rubber sheet. If combined normal and shearing forces are applied to the sensing surface, the conical feelers make contact with the acrylic board and are subjected to compressive and shearing deformation. The gray-scale value of the image of contact area is distributed as a bell shape, and since it is proportional to pressure caused on the contact area, it is integrated over the contact area to calculate the normal force. Lateral strain in the rubber sheet is caused by the horizontal component of the applied force and it makes the contact area with the conical feelers move horizontally. The horizontal displacement of the contact area is proportional to the horizontal component of the applied force, and is calculated as a centroid of the gray-scale value. Since the horizontal movement of the centroid has two degrees of freedom, both horizontal movement and contact area are used to detect the three components of the applied force.
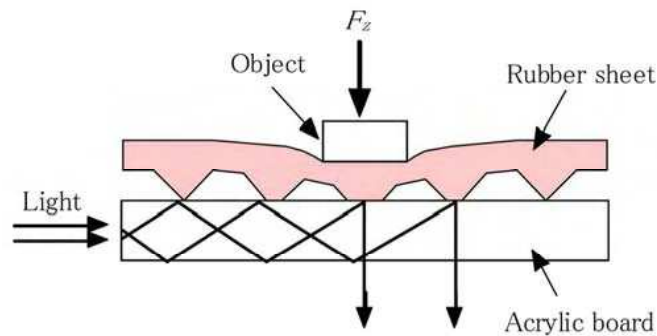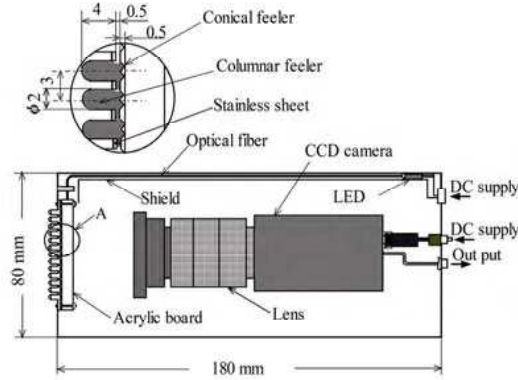

Fig. 1. Principle of an optical uni-axis tactile sensor.

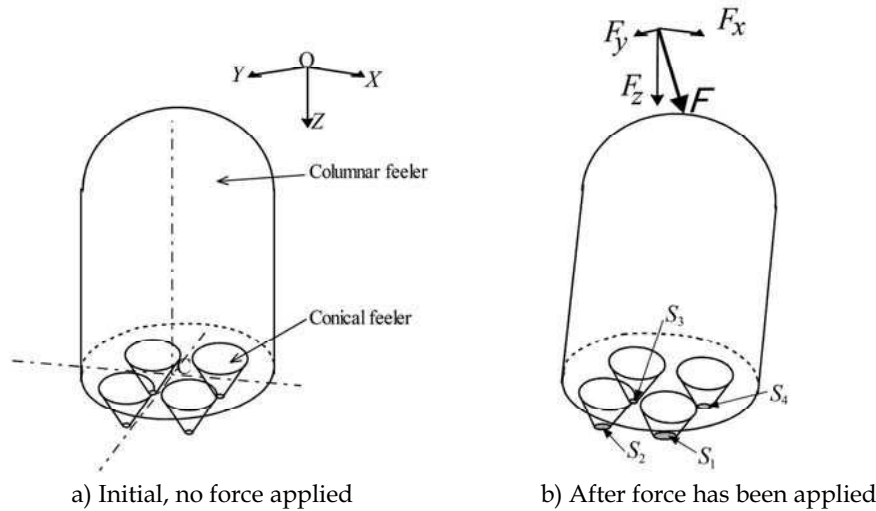Fig.2. One columnar and four conical feeler type three-axis tactile sensor.

a) Initial, no force applied   b) After force has been applied

Fig. 3.Three-axis force detection mechanism.

2.2 One Columnar and Four Conical Feelers Type

The schematic view shown in Fig. 2 demonstrates the structure of the tactile sensor equipped with sensing elements having one columnar and four conical feelers (Ohka, M. et al., 1995, 1996, 2004). This sensor consists of a rubber sheet, an acrylic plate, a CCD camera (Cony Electronics Co., CN602) and a light source. Two arrays of columnar feelers and conical feelers are attached to the detecting surface and the reverse surface of the sensor, respectively. The conical feelers and columnar feelers are made of silicon rubber (Shin-Etsu Silicon Co., KE1404 and KE119, respectively). Their Young's moduli are 0.62 and 3.1 MPa, respectively.

The sensing element of this tactile sensor comprises one columnar feeler and four conical feelers as shown in Fig. 3(a). The conical feelers and columnar feeler are made of silicon rubber. Four conical feelers are arranged at the bottom of each columnar feeler. If F_x, F_y and F_z are applied to press against these four conical feelers, the vertices of the conical feelers

collapse as shown in Fig. 3 (b). The F_x, F_y and F_z were proportional to the x-directional area-difference, A_x the A_y-directional area-difference, A_y and the area-sum, A_z respectively. The parameters A_x, A_y and A_z are defined below.

$$A_x = S_1 - S_2 - S_3 + S_4 \tag{1}$$

$$A_y = S_1 + S_2 - S_3 - S_4 \tag{2}$$

$$A_z = S_1 + S_2 + S_3 + S_4 \tag{3}$$

Under combined force, the conical feelers are compressed by the vertical component of the applied force and each cone height shrinks. Consequently, the moment of inertia of the arm length decreases while increasing the vertical force. Therefore, the relationship between the area-difference and the horizontal force should be modified according to the area-sum:

$$\begin{aligned} F_x &= (\alpha_{h0} - \alpha_h A_z) A_x \\ F_y &= (\alpha_{h0} - \alpha_h A_z) A_y \\ F_z &= \alpha_v A_z \end{aligned} \tag{4}$$

Fig. 4 .Robot equipped with the three-axis tactile sensor.

where, F_x, F_y and F_z are components of three-axis force applied to the sensing-element's tip. α_{h0}, α_h and α_v are constants determined by calibration tests.

The three-axis tactile sensor was mounted on a manipulator with five degrees of freedom as shown in Fig. 4, and the robot rubbed a brass plate with the tactile sensor to evaluate the tactile sensor. The robotic manipulator brushed against the brass plate with step-height δ = 0.1 mm to obtain the experimental results shown in Fig. 5. Figures 5(a), (b) and (c) show variations in Fz , Fx and the friction coefficient, μ , respectively. The abscissa of each figure is the horizontal displacement of the robotic manipulator. As shown in these figures, Fz and Fx jump at the step-height position. Although these parameters are convenient for presenting the step-height, the variation in Fz is better than that in Fx because it does not has a concave portion, which does not exist on the brass surface. Therefore Fz is adopted as the parameter to represent step-height.

It is noted that variation in the friction coefficient, μ , is almost flat while the robot was rubbing the tactile sensor on the brass plate at the step-height. This indicates that the tactile sensor can detect the distribution of the coefficient of friction because that coefficient should be uniform over the entire surface.
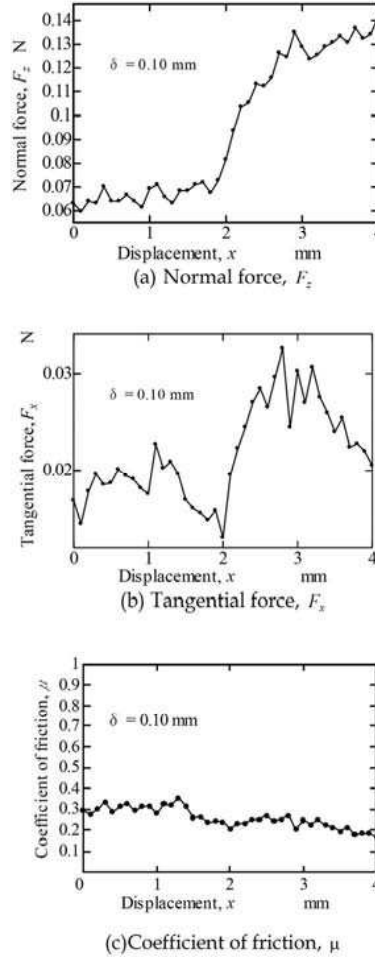
(a) Normal force, F_z

(b) Tangential force, F_x

(c)Coefficient of friction, μ

Fig. 5 Experimental results obtained from surface scanning.

2.3 None Columnar Feeler Type Three-axis Tactile Sensor for Micro Robots

In order to miniaturize the three-axis tactile sensor, the optical uni-axial tactile sensor is adopted as the sensor hardware because of simplicity and three-axis force is determined by image data processing of conical feeler's contact-areas to detect three-axis force (Ohka, M. et al., 1999, 2005a). The three-axis force detection principle of this sensor is shown in Fig. 6. To provide a definition for the force direction, a Cartesian coordinate frame is added to the figure. If the base of the conical feeler accepts three-axis force, it contacts the acrylic board, which accepts both compressive and shearing deformation. Because the light scatters on the contact area, the gray-scale value of the contact image acquired by the CCD camera distributes as a bell shape, in which the gray-scale intensity is highest at the centroid and decreases with increasing distance from the centroid.

It is found that the gray-scale $g(x, y)$ of the contact image is proportional to the contact pressure $p(x, y)$ caused by the contact between the conical feeler and the acrylic board, That is,

$$P(x, y) = C g(x, y), \tag{5}$$

where C and $g(x, y)$ are the conversion factor and the gray-scale distribution, respectively. If S is designated as the contact area of the acrylic board and the conical feeler, the vertical force, F_z is obtained by integrating the pressure over the contact area as follows:

$$F_z = \int_S p(x, y) dS . \tag{6}$$

If Eq. (5) is substituted for Eq. (6),

$$F_z = \int_S C g(x, y) dS \equiv C G , \tag{7}$$

where the integration of $g(x, y)$ over the contact area is denoted as G.

Next, to formulate horizontal components of the force vector F_x and F_y, x- and y- coordinates of the centroid of gray-scale value, (X_G, Y_G) are calculated by

$$X_G = \frac{\int_S g(x, y) x dS}{\int_S g(x, y) dS} , \tag{8}$$

and

$$Y_G = \frac{\int_S g(x, y) y dS}{\int_S g(x, y) dS} . \tag{9}$$

In the integrations, the integration area S can be enlarged as long as it does not invade adjacent contact areas, because g(x, y) occupies almost no space outside contact area. Since the shearing force induces axial strain in the silicon rubber sheet, the contact area of the conical feeler moves in the horizontal direction. The x- and y-components of the movement are denoted as u_x and u_y, respectively. They are variations in the abovementioned X_G and Y_G:

$$u_x = X_G^{(t)} - X_G^{(0)}, \tag{10}$$

$$u_y = Y_G^{(t)} - Y_G^{(0)}, \tag{11}$$

where the superscripts (t) and (0)represent current and initial steps, respectively.

If friction between the silicon rubber and the acrylic board is ignored, x- and y- directional forces, F_x and F_y are calculated as follows:

$$F_x = K_x u_x, \tag{12}$$

$$F_y = K_y u_y, \tag{13}$$

where K_x and K_y are x- and y-directional spring constants of the rubber sheet, respectively.

Here we examine the relationship between the gray-scale value of the contact image and contact pressure on the contact area to validate the sensing principle for normal force. In the investigation FEM software (ABAQUS/Standard, Hibbitt, Karlsson & Sorensen, Inc.) was used and contact analysis between the conical feeler and the acrylic board was performed. Figure 7(a) shows a mesh model of the conical feeler generated on the basis of the obtained morphologic data; actually, the conical feeler does not have a perfect conical shape, as shown in Fig. 7(a). The radius and height of the conical feeler are 150 and 100 µ m, respectively.
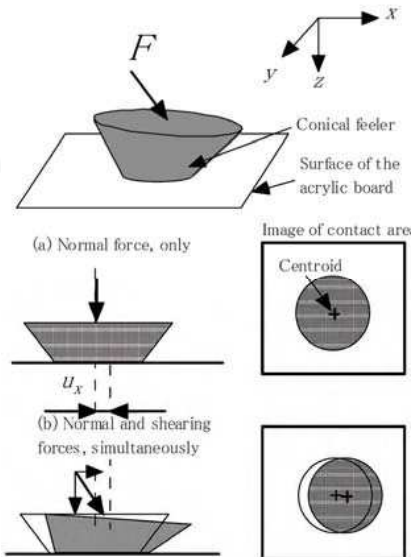
Fig. 6. Principle of a none columnar type three-axis tactile sensor.
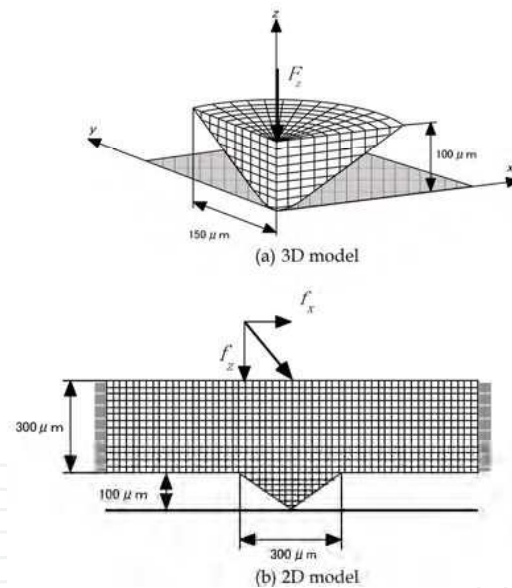

Fig. 7. Models for FEM analysis.

The Young's modulus of the silicon rubber sheet was presumed to be 0.476 Mpa. The Poisson's ratio was assumed to be 0.499 because incompressibility of rubber, which is assumed in mechanical analysis for rubber, holds for the value of Poisson's ratio. Only one quarter of the conical feeler was analyzed because the conical feeler is assumed to be symmetric with respect to the z-axis. Normal displacements on cutting planes of x-z and y-z were constrained to satisfy the symmetrical deformation, and the acrylic board was

modeled as a rigid element with full constraint. The three-dimensional (3-D) model was used for a precise simulation in which a normal force was applied to the top surface of the conical feeler. In the previous explanation about the principle of shearing force detection, we derived Eqs. (12) and (13) while ignoring the friction between the conical feeler and the acrylic board. In this section, we analyze the conical feeler's movement while taking into account the friction to modify Eqs. (12) and (13). Figure 7(b) shows a 2-D model with which we examine the deformation mechanism and the conical feeler movement under the combined loading of normal and shearing forces.

In the 2-D model, the same height and radius values for the conical feeler are adopted as those of the previous 3-D model. The thickness of the rubber sheet is 300 μ m and both sides of the rubber sheet are constrained. Young's modulus and Poisson's ratio are also adopted at the same values as those of the previous 3-D model. The acrylic board was modeled as a rigid element with full constraint as well. The coefficient of friction between the conical feeler and the acrylic board is assumed to be 1.0 because this is a common value for the coefficient of friction between rubber and metal. The critical shearing force, τ_{max} , which means the limitation value for no slippage occurring, is presumed to be 0.098 Mpa.
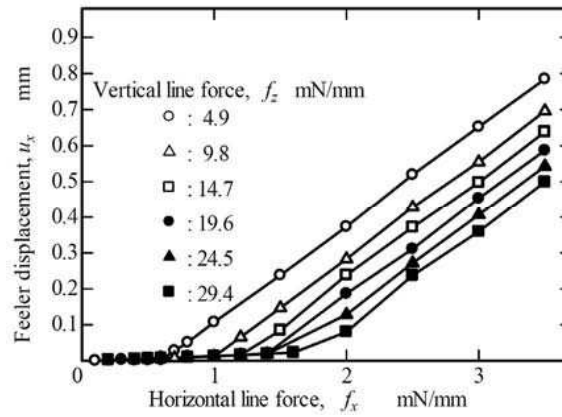

Fig. 8. Relationship between horizontal feeler movement and horizontal line force.

Combined loadings of normal and shearing forces were applied to the upper surface of the rubber sheet. The conical feeler's movement, u_x, was calculated with Eq. (10) while maintaining the vertical component of line force f_z, a constant value, and increasing the horizontal component of line force f_x, where the components of line forces f_y and f_z are x- and z-directional force components per depth length, respectively. Since the conical feeler's movement is calculated as movement of the gray-scale's centroid in the later experiments, in this section it is calculated as the movement of the distributed pressure's centroid.

Figure 8 shows the relationships that exist between the movement of the centroid of the distributed pressure, u_x, and the horizontal component of the line force, f_x. As shown in that figure, there are bi-linear relationships where the inclination is small in the range of the low-horizontal line force and becomes large in the range of the high-horizontal line force, exceeding a threshold. This threshold depends on the vertical line force and increases with increasing vertical line force, because the bi-linear relationship moves to the right with an increase in the vertical line force.

The abovementioned bi-linear relationship can be explained with the Coulomb friction law

and elastic deformation of the conical feeler accepting both normal and shearing forces. That is, the conical feeler accepts shearing deformation while contacting the acrylic board when shearing stress arising between the acrylic board and conical feeler does not exceed a resolved shearing stress. At this stage of deformation, since the contact area changes from a circular to a pear shape, the centroid of distributed pressure moves in accordance with this change in contact shape. The inclination of the relationship between u_x and f_x is small in the range of a low loading level due to the tiny displacement occurring in the abovementioned deformation stage. In the subsequent stage, when the shearing stress exceeds the resolved shearing stress τ_{max}, then according to the increase of the lateral force, the friction state switches over from static to dynamic and the conical feeler moves markedly due to slippage occurring between the conical feeler and the acrylic board. The inclination of u_x -f_x, therefore, increases more in the range of a high shearing force level than in the range of a low shearing force.

Taking into account the abovementioned deformation mechanism, we attempt to modify Eqs. (12) and (13). First, we express the displacement of centroid movement at the beginning of slippage as u_{x1}. If $u_x = u_{x1}$ is adopted as the threshold, the relationship between u_x and F_x is expressed as the following two linear lines:

$$F_x = \beta_x u_x \quad (u_x < u_{x1}),$$ (14)

$$F_x = K_x(u_x - u_{x1}) + \beta_x u_{x1} \quad (u_x \geq u_{x1}),$$ (15)

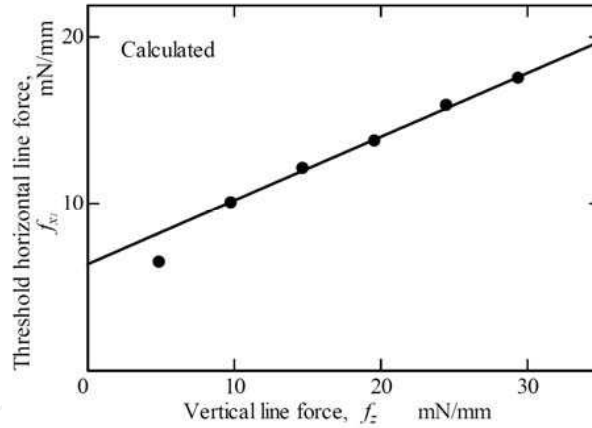where β_x is the tangential directional spring constant of the conical feeler.

Fig. 9. Relationship between threshold of horizontal line force and vertical line force.

Second, the relationship between the horizontal line force at bending point f_{x1} and the vertical line force, f_z, is shown in Fig. 9. As is evident from this figure, f_{x1} versus f_z is almost linear in the region covering f_x =10 mN/mm. In the present paper, we assume the obtained relationship approximates a solid linear line in Fig. 9. If we denote horizontal force corresponding to u_{x1} as F_{x1}, F_{x1} is expressed as following equation:

$$F_{x1} = \alpha_x F_z + \gamma_x,$$ (16)

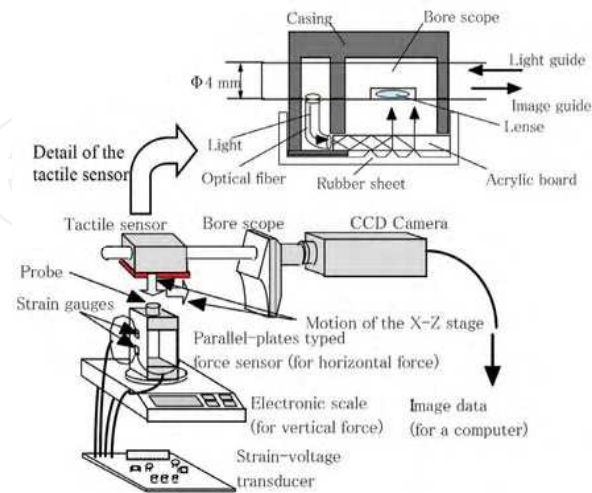where a_x and γ_x are constants identified from F_z versus F_{x1}.

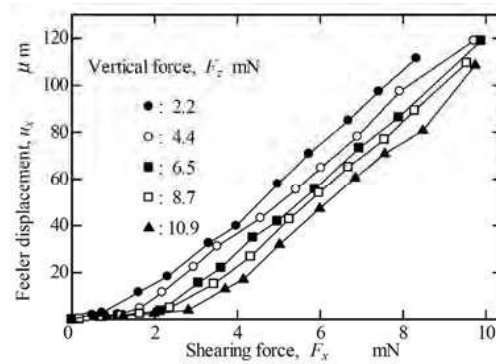Fig. 10. A micro three-axis tactile sensor system.

Fig. 11. Relationship between horizontal displacement of the conical feeler and shearing force.
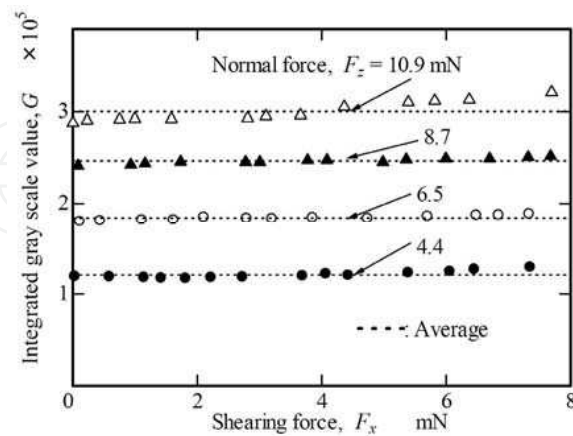

Fig. 12. Variation in integrated gray scale value under applying shearing force.

An experimental tactile sensing system is shown in Fig. 10. Light emitted from a light source in the bore scope is introduced into one side of the acrylic board, functioning as an optical waveguide. Distributed light spots caused by contact with conical feelers on the rubber sheet and the acrylic board are detected by the CCD camera through the bore scope and are accumulated into the frame memory board built into the computer. The normal force applied to the sensing surface of the tactile sensor is measured by an electric scale (resolution: 0.1 mN) and is sent to the computer through an RS232C interface. The shearing force is measured by a load cell created through our own work. The load cell consists of a pair of parallel flat springs with four strain gauges plastered to their surfaces and was calibrated with the electric scale. Two-dimensional force is applied to the sensing surface of the tactile sensor with the adjustment of a precision feed screw of the X-Z stage.

In order to evaluate Eqs. (14) to (16), after applying the initial normal force onto the sensing surface, F_x was increased in a stepwise manner while maintaining a constant normal force. Upon each increase in force, the centroid of gray-scale values within the aforementioned sub-window was calculated and the displacement of the centroid from the initial position was called u_x. In Fig. 11, the ordinate and abscissa represent the horizontal force, F_x, and the centroid displacement, u_x, respectively. As is evident from Fig. 11, the low- and high-load regions exhibit different sensitivity coefficients. This is a similar inclination to the simulated results discussed in Fig. 8.

Finally, we show variation in G under a stepwise increase of F_x and constant F_z in Fig. 12 to determine whether the relationship between G and F_z is not influenced by a variation in F_x. In fact, Fig. 12 indicates that G maintains a constant value even if F_x increases. Figure 13 shows a comparison between relationships of G -F_z with shearing force and without shearing force. In Fig. 13 the solid circles represent the relationship with the shearing force obtained from Fig. 12, and it is clear that both of the relationships almost coincide in Fig. 13. Since the magnitude of the shearing force has no influence on the sensitivity characteristic in the normal direction, it is possible to identify the shearing force and normal force independently.
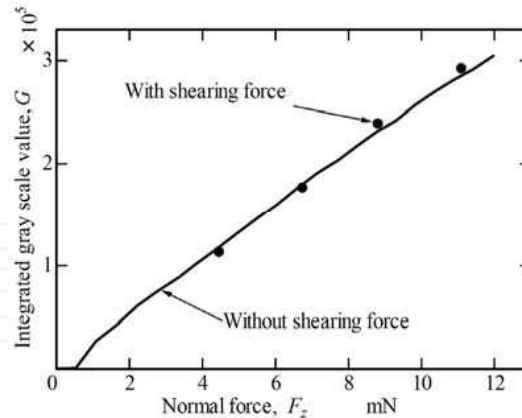

Fig. 13. Relationship between normal force and integrated gray scale value.

2.4 Hemispherical Three-axis Tactile Sensor for Robotic Fingers

On the basis of the aforementioned two examples of three-axis tactile sensors, a hemispherical tactile sensor was developed for general-purpose use. The hemispherical

tactile sensor is mounted on the fingertips of a multi-fingered hand (Ohka, M. et al., 2006). Figure 14 shows a schematic view of the present tactile processing system to explain the sensing principle. In this tactile sensor, the optical waveguide dome is used instead of the waveguide plate, which is used in the previously described tactile sensors. The light emitted from the light source is directed into the optical waveguide dome.
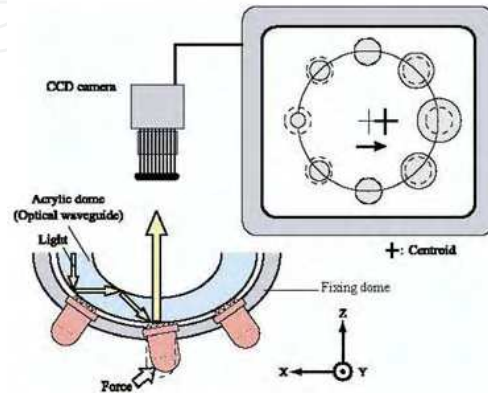

Fig. 14. Principle of the hemisherical tactile sensor system.
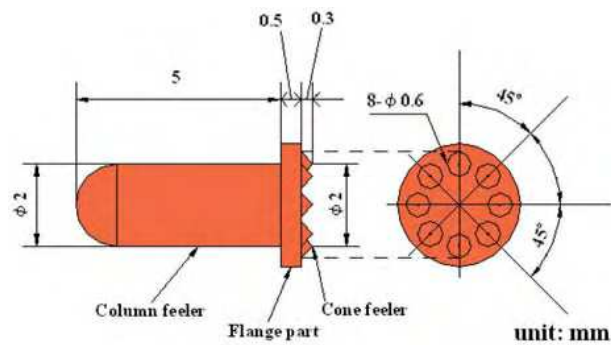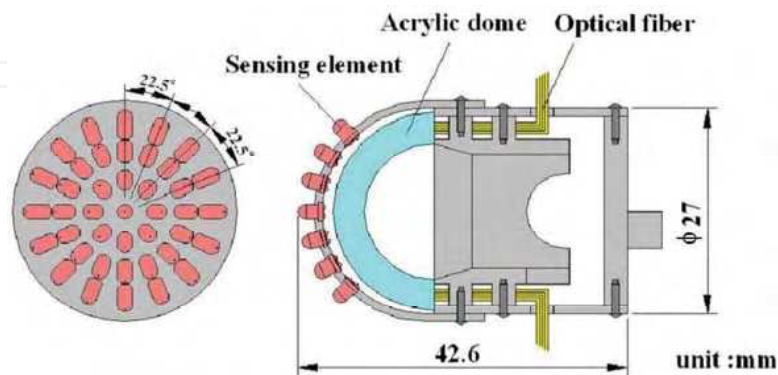

Fig. 15. Sensing element of eight feeler type.

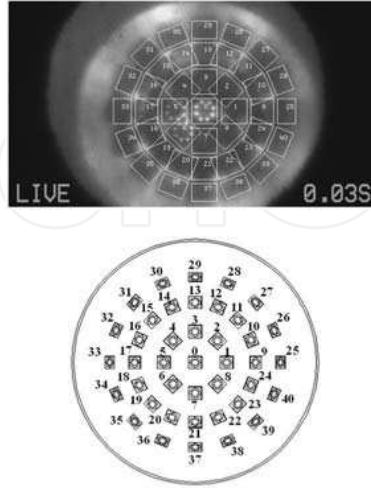Fig. 16. Fingertip including the three-axis tactile sensor.

Fig. 17. Address of sensing elements

The sensing element presented in this paper comprises a columnar feeler and eight conical feelers as shown in Fig. 15. The sensing elements are made of silicone rubber, as shown in Fig. 14, and are designed to maintain contact with the conical feelers and the acrylic dome and to make the columnar feelers touch an object. Each columnar feeler features a flange to fit the flange into a counter-bore portion in the fixing dome to protect the columnar feeler from horizontal displacement caused by shearing force.

When three components of force, the vectors F_x, F_y and F_z, are applied to the tip of the columnar feeler, contact between the acrylic board and the conical feelers is measured as a distribution of gray-scale values, which are transmitted to the computer. Since the contact mechanism between the acrylic dome and conical feelers is difference from the case of flat acrylic board, relationships between the shearing force and centroid displacement and between the normal force and integrated gray scale value cannot be approximated with linear functions as shown in Eqs. (7), (12) and (13). The F_x F_y and F_z values are calculated using the integrated gray-scale value G and horizontal displacement of the centroid of the gray-scale distribution $u = u_x\, \mathbf{i} + u_y\, \mathbf{j}$ as follows:

$$
\begin{aligned}
F_x &= f(u_x), \\
F_y &= f(u_y), \\
F_z &= g(G),
\end{aligned}
\tag{17}
$$

where $\mathbf{i}$ and $\mathbf{j}$ are orthogonal base vectors of the x- and y-axes of a Cartesian coordinate, respectively; $f(x)$ and $g(x)$ are approximate none-linear curves estimated in calibration experiments.

We are currently designing a multi-fingered robotic hand for general-purpose use in robotics. The robotic hand includes links, fingertips equipped with the three-axis tactile sensor, and micro-actuators (YR-KA01-A000, Yasukawa). Each micro-actuator consists of an AC servo-motor, a harmonic drive, and an incremental encoder, and is developed particularly for application to a multi-fingered hand. Since the tactile sensors should be fitted to the multi-fingered hand, we are developing a fingertip to include a hemispherical three-axis tactile sensor. That is, the fingertip and the three-axis tactile sensor are united as shown in Fig. 16.

The acrylic dome is illuminated along its edge by optical fibers connected to a light source. Image data consisting of bright spots caused by the feelers' collapse are retrieved by an optical fiber-scope connected to the CCD camera as shown in Fig. 17.
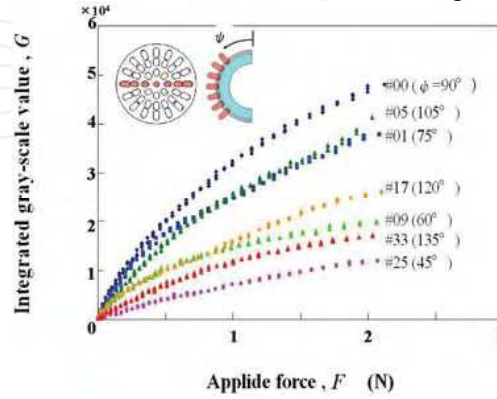

Fig. 18. Relationship between applied force and gray-scale value.
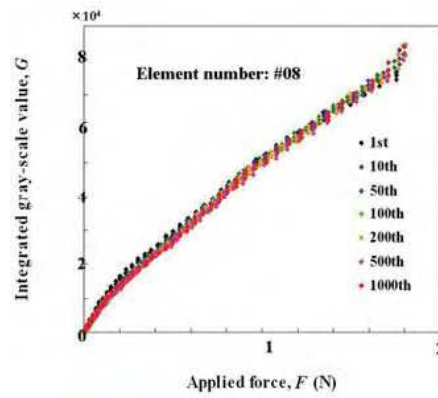

Fig. 19. Repeatability of relationship between integrated gray-scale value and applied force.
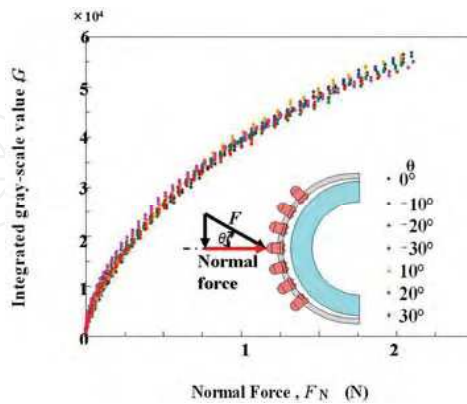

Fig. 20. Relationship between integrated gray-scale value and applied normal force at several inclinations.

To evaluate the sensing characteristics of sensing elements distributed on the hemispherical dome, we need to measure the variation within the integrated gray-scale values generated by the sensor elements. Figure 18 shows examples of variation in the integrated gray-scale value caused by increases in the normal force for sensors #00, #01, #05, #09, #17, #25 and #33. As the figure indicates, the gradient of the relationship between the integrated gray-scale value and applied force increases with an increase in φ; that is, the sensitivity depends upon the latitude on the hemisphere. Dome brightness is inhomogeneous because the edge of the dome is illuminated and light converges on the parietal region of the dome. The brightness is represented as a function of the latitude φ, and since the sensitivity is uniquely determined by the latitude, it is easy to modify the sensitivity according to φ.

The relationship between the integrated gray-scale value and applied force has high repeatability. Experimental results from 1,000 repetitions on #00 are superimposed in Fig. 19, which shows that all the curves coincide with each. The deviation among them is within 2%.

Normal force F_N and shearing force F_S applied to the sensing elements are calculated using the following formulas.

$$F_N = F \cos \theta \tag{18}$$
$$F_S = F \sin \theta \tag{19}$$

With Eq. (18) we obtained the variation in the integrated gray-scale values and applied normal force. Figure 20 displays the relationship for #00. Even if the inclination is varied from -30° to 30°, the relationship coincides within a deviation of 3.7%.

When force is applied to the tip of the sensing element located in the parietal region under several θ s, relationships between the displacement of the centroid and the shearing-force component calculated by Eq. (19) are obtained as shown in Fig. 21. Although the inclination of the applied force is varied in the range from 15° to 60°, the curves converge into a single one. Therefore, the applied shearing force is obtained independently from displacement of the centroid.
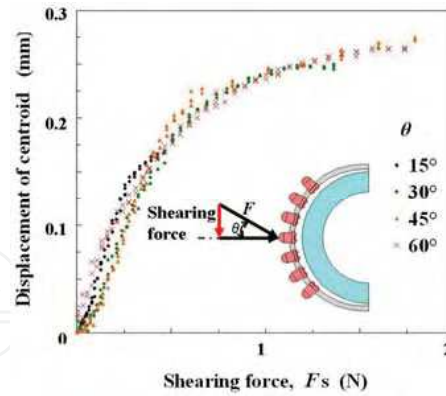

Fig. 21. Relationship between displacement of centroid and applied shearing force.

3. Human mimicking Tactile Sensing

3.1 Human Tactile Sensation

Human beings can recognize subtle roughness of surfaces by touching the surfaces with their fingers. Moreover, the surface sensing capability of human beings maintains a

relatively high precision outside the laboratory. If we can implement the mechanisms of human tactile sensation to robots, it will be possible to enhance the robustness of robotic recognition precision and also to apply the sensation to surface inspection outside the laboratory. Human tactile recognition is utilized as a model of robotic tactile regognition (Ohka, M. et al., 2005b). Human tactile recognition ability has been examined using psychophysical experiments and microneurography. Consequently, mechanoreceptors of skin are classified into four types according to response speed and receptive field size (Vallbo, Å. B. & Johansson R. S., 1984). In the present paper, we focus our discussion on FA I (First adapting type I unit) because FA I responds to surface roughness. In regard to remarks related to FA I obtained by the authors and other researchers, remarks used for the present formulation are summarized as follows:
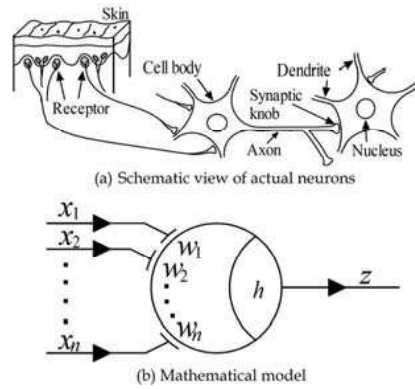

Fig. 22. Modeling of fast adaptive Type I mechanoreceptive unit.

(1) FA I responds to the first-order differential coefficient of mechanical stimulus varying with time (Moss-Salentijin, L., 1992; Miyaoka, T., 1994).
(2) Acquirable physical stimuli of FA I are surface roughness of several tens of microns in amplitude, and mechanical vibration of several microns in amplitude and several tens of Hz in frequency (Miyaoka, T., 1994).
(3) Human subjects feel moving fine step height more strongly at high scanning speeds than at low scanning speeds (Kawamura, T. et al., 1998)
(4) The mechanoreceptors related to FA I are Meissner's corpuscles(Moss-Salentijin, L., 1992; Miyaoka, T., 1994).

3.2 Neuron model
Neurophysiology studies have clarified that the mechanoreceptive units comprise a few mechanoreceptors accepting mechanical stimuli and a sensory nerve fiber transmitting sensory signals. In the present paper, a neuron processing the sensory signals is treated as an element of the unit in order to consider the unit as comprising mechanoreceptors, a sensory nerve fiber and a neuron in the brain. If we make a model of the tactile nerve system on the basis of neural network models, it is easy to incorporate the above-mentioned human tactile mechanism into robotics.
The McCulloch-Pitts model (McCulloch, W. & Pitts, W., 1943) is adopted here as the mechanoreceptive unit, while the afore-mentioned remarks on human tactile sensations are formulated to obtain expressions of the fine surface roughness recognition mechanism.

Figure 22 shows a neural network related to the tactile sensory system. When mechanical stimuli are applied to the surface of the skin, the mechanoreceptors accept the stimuli and emit a voltage signal. The signal is transmitted to a dendrite extending from a neuron through a synaptic connection. The arrival of the output signal from the mechanoreceptor effects a change in the membrane potential inside neuron. If several signals from mechanoreceptors arrive almost simultaneously at the neuron, these signals are superimposed in the neuron and summation of these signals change the membrane potential. This effect is called spatial summation and is modeled first.

The neuron accepts n-signals $x_1, x_2, \ldots , x_n$ emitted from n-mechanoreceptors distributed in the skin. The weight of the synaptic connection between i-th mechanoreceptor and the neuron is represented as w_i. Taking into account the spatial summation, the membrane potential, u is calculated as

$$u = \sum_{i=1}^{n} w_i x_i .$$
(20)

The mechanoreceptor seems to detect the time derivative of skin deformation according to Remark (1) in the previous section, where it is assumed that the mechanoreceptor detects the strain rate caused in the skin and that it emits signals proportional to the magnitude of the strain rate. Namely, the output of the i-th mechanoreceptor, x_i of Eq.
(20) is calculated by the following expression,

$$x_i = a \left| \frac{d\varepsilon_i}{dt} \right| ,$$
(21)

where ε_i is the compressive strain of the i-th mechanoreceptor and a is a coefficient.

When an output signal emitted from the mechanoreceptor arrives to the neuron, a change occurs in the membrane potential. If the next signal arrives at the neuron before the change attenuates and vanishes, the next signal is superimposed on the residual of the preceding signal. This effect is called *time summation* (Amari, T., 1978) and is formulated as convolution integral of $w_i (t - t') x (t')$ with respect to t' from the past to the present t if the weight of synaptic connection between the i-th mechanoreceptor and the neuron is represented as $w_i (t')$ at time t' . Consequently, by incorporating the time summation into Eq. (20), the membrane potential u is calculated as

$$u = \sum_{i=1}^{n} \int_{-\infty}^{t} w_i(t - t') x_i(t') dt' .$$
(22)

Influence of signal arrival on the membrane potential degreases with late of the signal arrival. This effect is expressed as degreasing the synaptic potential, $w_i (t)$. However, there are no available data on variation in the synaptic potential. In the present paper, it is assumed that $w_i (t)$ varies as square wave; namely it takes a constant value during 0 to τ sec, after which it takes 0.

$$w_i(t) = \begin{cases} 1, & 0 \leq t < \tau \\ 0, & t < 0 \end{cases} .$$
(23)

It is known that neurons have the threshold effect where the neuron emits an output if the membrane potential, u expressed as Eq. (24), exceeds a threshold, h . The output is a pulse signal and the pulse density of the signal is proportional to the difference between membrane potential u and threshold h . The pulse density of the signal is expressed as z , while the threshold function,

φ (*q*) is designated to formulate the threshold effect. The pulse density, *z* is,

$$z = \phi(u - h) \qquad (24)$$

$$\phi(q) = \begin{cases} q, q \geq 0 \\ 0, q < 0 \end{cases}. \qquad (25)$$

As mentioned above, data processing of the mechanoreceptive type FA I unit is formulated using a mathematical model for neuron-incorporated spatial and time summations. In the following sections, we confirm these expressions are by numerical simulation using FEM analysis of a human finger and experiments using an articulated robot installed in the present neural model.

3.3 Simulation

As mentioned in Remark (4), the mechanoreceptor of FA I appears to be Meissner's corpuscle. In order to evaluate the present mathematical model derived in the preceding section, we performed a series of FEM analyses using a mesh model as shown in Fig. 23. In the present mesh model, a human finger is expressed as a half cylinder. Normal strain, ε_z arises at the existing potion of Meissner's corpuscle, calculated when the finger is slid along a flat surface having s fine step height. We selected δ=5 , 7.5 , 10 , 12.5 and 15 μ m as the step heights to compare experimental results obtained by psychophysical experiments.

It is possible that viscoelastic deformation of the skin causes the scanning speed effect described in Remark (3). In this paper, we adopt the first-order Prony series model (ABAQUS Theory manual, 1998) which is equivalent to the three-element solid, as the viscoelestic model to approximate the skin's viscoelastic behavior.
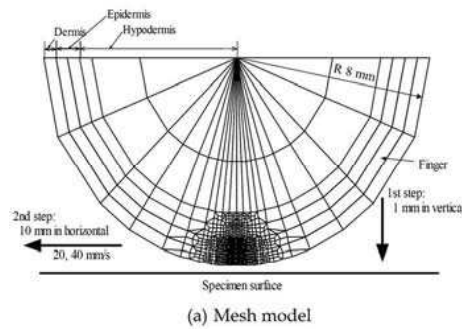
(a) Mesh model
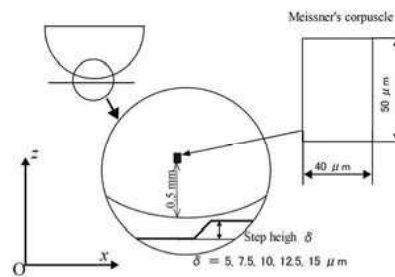
(b) Detail of the contact portion

Fig. 23. Mesh model for contact analysis.

Human skin is composed of three layers: the epidermis, the dermis, and the hypodermis. Young's moduli of these three layers are assumed to be 0.14, 0.034 and 0.080 Mpa (Maeno, T. et al., 1998). On the other hand, the Poisson ratios of all layers are assumed to take same value of 0.45 because there are no reports concerned with it. Moreover, this value is reasonable if the skin has similar mechanical characteristics to rubber. Since there are no data on the ratio of the shearing modulus's initial value to its terminal value and the ratio between the bulk modulus' initial value and its terminal value for human skin, a common value of 0.5 for the three layers is assumed and a value of 12.9 msec (Oka, H. & Irie, T., 1993) is adopted as the time constant.

The present mesh model was compressed upon a flat rigid surface having a fine step height and slid over the surface. Then, we obtained the y-directional normal strain, ε_y in the Meissner's corpuscle, shown by a solid square in Fig. 23. The mesh element of Meissner's corpuscle is located 0.5 mm below the skin surface. The width and height of the element are 40 μ m and 50 μ m, respectively.

In the present loading history, the modeled finger was initially moved 1 mm in the negative perpendicular direction and compressed upon the flat surface. Subsequently, it was slid 10 mm in the horizontal direction. Any compressive deformation produced during the first step of the loading history should be diminished to allow evaluation of the stimulus of the fine step height caused by the scanning motion only. Therefore, after contact was established between the finger and the rigid flat surface, the finger was stabilized for 1 sec to diminish the effect of compressive deformation. Furthermore, we selected v = 20 mm/s and 40mm/s for the finger sliding speed to simplify comparison between simulated and experimental results of psychophysical experiments conducted in our previous works. We selected 0 for the coefficient of friction between the finger and the rigid surface.
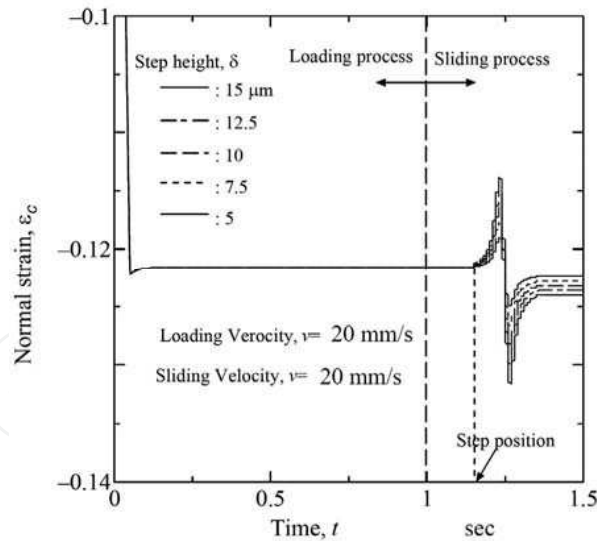

Fig. 24. Variation under compressive strain.

Next, we substituted the normal strain, ε_z obtained from the above-mentioned FEM analysis, into Eq. (21) by putting ε_z to ε_c. Subsequently, Eqs. (20)-(25) were calculated to obtain simulated signals emitted by FA I. Although the constants included in Eqs. (20)-(24), a , n , τ

and *h* should be determined by neurophysical experiments, we could not obtain such data. We assumed the values of these constants as follows. Here, *a* , the proportionality constant of relationship between output signal and stimulus magnitude, was presumed to be *a* = 1 Vsec. We were attempting to evaluate the simulation by normalizing outputs of the present model with the highest peak value among the outputs of different conditions. Since the plane strain condition was assumed in the present simulation, it was equivalent to a simulation of Meissner's corpuscles aligned in the depth direction of this sheet and having the same characteristics. To abbreviate the present analysis, the variance among mechanoreceptive units was ignored and *n* = 1 was presumed. Since the afore-mentioned dependence of speed on step height recognition seems closely related to temporal summation, we calculated several time constants within a range of τ= 10 ∼ 300 msec. Following that, we selected the best τ that could best fit our experimental results. Since threshold *h* does not affect our simulated results, we summed *h* = 0 V.

Figure 24 shows the variation in normal strain of the position of Meissner's corpuscle as depicted in Fig. 23. Since the finger remains stational for 1 sec to erase the history of the initial compressive strain, the variation remains at an almost constant value following the transient variation occurring at the initial stage. Then, when the fine step height comes near the position of Meissner's corpuscle, two prominent spikes arise. The figure also indicates that the magnitude of the spike increases with an increase in step height.
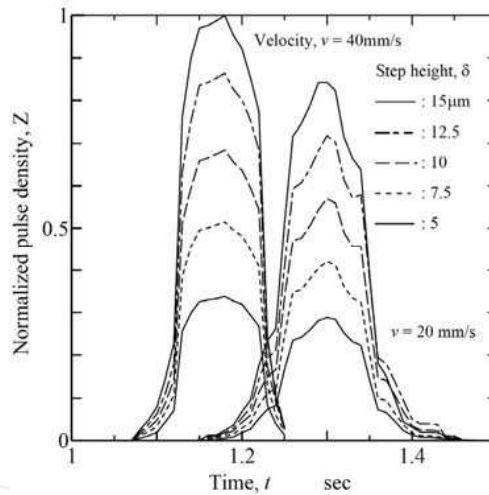

Fig. 25. Variation in normalized pulse density.

As mentioned in the previous section, we calculated several time constants within a range of τ= 10 ∼ 300 msec. First, we will examine variation in normalized pulse density at τ= 300 msec. The strain rate calculated from the normal strain shown in Fig. 24 is substituted into the present mathematical model presented by Eqs. (20)-(25) to obtain the pulse density, *z* . Since we designated *a*= 1 as a value of the constant included in Eq. (2), the obtained pulse density *z* does not have any physical meaning. Hence, a comparison between calculated results under different conditions should be performed with a ratio. Here, the calculated pulse density is normalized as a peak of the calculated pulse density below *v* = 40 mm/s, and δ= 15 μ m is designated 1. In Fig. 25 the results are normalized according to the above-

mentioned procedure.

For both v = 20 mm/s and 40 mm/s, results show that normalized pulse density increases with the reach of the mechanoreceptor to fine step heights, and that their maximum values increase with an increase in step height, δ . In order to examine the influence of a finger's sliding speed and step height on pulse density, we obtained the maximum value for each simulation condition. Figure 26 illustrates the relationship between maximum pulse density and step height for v = 20 mm/s and 40mm/s.

The figure shows that the maximum pulse density is proportional to step height. If we compare pulse densities of different finger sliding speeds at the same step height to examine the influence of a finger's sliding speed on pulse density, we find the pulse density at a high finger speed is higher than at a low finger speed.

Next, to estimate a proper value of τ , we performed the same calculations (except for the value of τ) under the same calculation conditions as the calculation shown in Fig. 25.
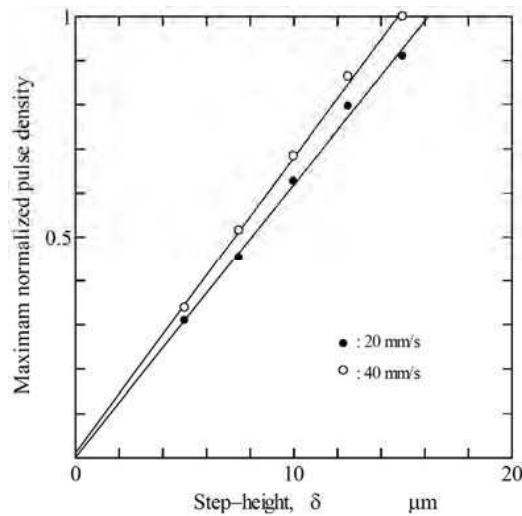

Fig. 26. Relationship between model output and step-height.

To obtain a conversion factor from the pulse density to the accepted step height, we obtained regression coefficients of calculated results for v = 20 and 40 mm/sec and adopted the mean value of the regression coefficient as the conversion factor. After employing this factor, the ordinate of Fig. 26 was transformed to an accepted step height, relationships between simulated step height and accepted step height were obtained, as shown in Fig. 27. The symbols in Fig. 27 show our experimental results (Ohka, M. Et al., 2004) obtained from a series of psychophysical experiments. This figure demonstrates that even if human subjects recognize the same step height, they feel that a given step height is higher at a high finger speed than at a low speed. Furthermore, on comparing calculated results with experimental results, we find that the calculated results coincide well with the experimental results below τ = 300 msec.

3.4 Application to robotics

The robotic manipulator shown in Fig. 4 rubbed a brass plate with the tactile sensor's sensing surface to obtain surface data of the brass plate. To enable the robotic manipulator

to traverse the brass plate correctly, it is possible to adjust the horizontal datum of the brass plate with three screws attached to it at intervals of 120°. We prepared three brass plates having step heights of δ= 05.0 , 0.1 , 0.2 mm, and one brass plate having no step height (δ = 0 mm).

During the surface scanning test,

(1) we maintained contact between the tactile sensor's sensing surface and brass plate, and had the sensing surface press on the brass plate to apply an initial vertical force to the sensing element;

(2) the robotic manipulator traversed the brass plate in horizontal movement of 10 mm.

As a result, we obtained $\Delta U_z = U_z - U_{z0}$, which is the difference between the current vertical displacement and the initial vertical displacement, U_{z0}.
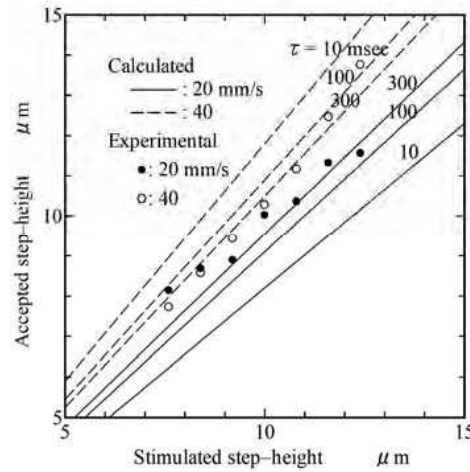

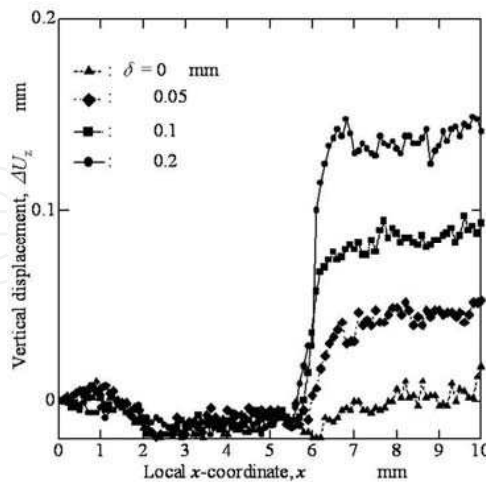Fig. 27. Comparison of simulated results and experimental results.
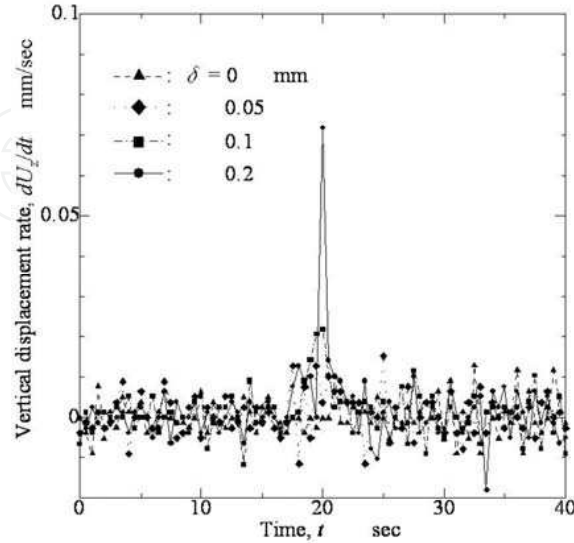

Fig. 28. Variation in vertical displacement.

Fig. 29. Variation in rate of vertical displacement.

Figure 28 shows variation in the vertical displacement measured by the sensing element. The abscissa and ordinate of Fig. 28 are the local x-coordinates of the robotic manipulator's end-effecter and the difference between the current vertical displacement and initial vertical displacement, ΔU_z, respectively. The origin of the abscissa corresponds to the position where the robotic manipulator applied the initial vertical force to the tactile sensor. Figure 28 shows that ΔU_z jumps at the step-height position, and that the jump heights increase with increasing step height. Furthermore, according to Fig. 28, the experimental results vary according to the step: if the step-height magnitudes of the experimental results are examined, it is found that the ratio is about 1:2:5, a ratio that approximates the ratio of the step heights formed on the brass plates (1:2:4). Therefore, the sensor can detect step heights formed on the surface of an object. However, if we intend to measure the step height from variations in the vertical displacement ΔU_z , then the initial displacement U_{z0} should be constant because it is used as a datum for step-height measurement. In the case of robotics, the sensing surface of the tactile sensor often repeats touching and detaching from the object surface. Furthermore, there is no guarantee that the sensing surface faces parallel to the object surface; for step-height sensing, it is preferable that the step height is estimated from the current values.

As a candidate for the current physical quantity excluding the vertical displacement, U_z, we attempt to consider the time derivative of vertical displacement, $\dot{U}_z$. Figure 29 shows the variation in $\dot{U}_z$. The abscissa represents the time elapsed from begin of the scan just z after initial load is applied. In Fig. 29, $\dot{U}_z$ has a peak value corresponding to the position of step height. Since U_z is determined from the current value obtained from the measurement, it appears more suitable than ΔU_z for robotic real-time step-height recognition, though it

depends on the value of U_{z0}. However, since $\dot{U}_z$ contains many noise components, it is difficult to discriminate step heights of δ = 0.05 mm and 0.1 mm. Therefore, $\dot{U}_z$ holds no advantage for fine discrimination of step height.
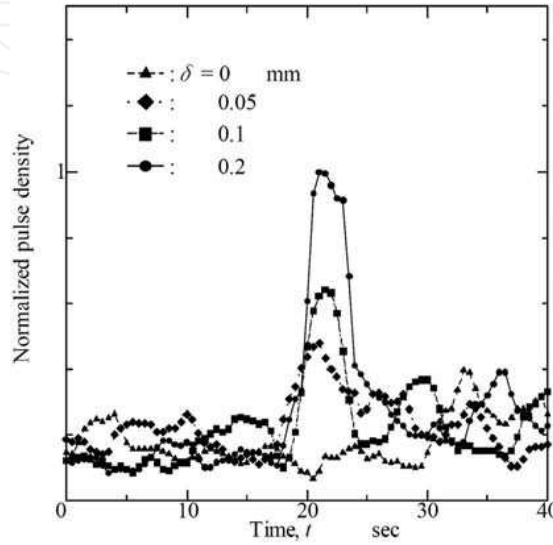

Fig. 30. Variation in pulse density

Next, the present model was incorporated into the robotic manipulator's surface-recognition system. The variation in the time derivative of vertical displacement of the present tactile sensor in Fig. 29, $\dot{U}_z$ is divided by a representative length of the tactile sensor to obtain the strain rate substituted into Eq. (21). The strain rate becomes an input signal of the present model and is used to derive pulse density, z with Eq. (24). In this calculation, we employed the following constants included in the model: a= 1 Vsec, n = 1, τ= 3 sec, h= 0 V.

In estimating the time constant, τ , we considered the difference of time consumption for data processing between human tactile sensation and robotic tactile recognition. Namely, since image-data processing is required to obtain tactile data in the present tactile sensor, sampling time is rather long at 0.5 sec. In contrast, FA I's band of tactile frequency is approximately several tens of Hz, and is one digit larger that the tactile sensor's band. Therefore, in calculating the present model, we used a value ten times larger than the τ= 300 msec in Fig. 27.

Figure 30 illustrates the output of the present model. In this figure , the ordinate shows a normalized pulse density with its maximum value at a step height of 0.2 mm, while variation in the normalized pulse density, Z shows a single peak value. Furthermore, it is easy to distinguish the difference between the cases of δ = 0.05 mm and 0.1 mm due to the noise-filtering effect of the present model. This discrimination was impossible in Fig. 29. As a result, we confirm that the present model is effective for robotic recognition of fine surface step heights in real time.

4. Conclusion

In this chapter, mechanism and evaluation of the optical three-axis tactile sensor are described to show sensing characteristics on three components of force vector applied to the sensing element. Then, recognition method for subtle convex portions of flat plate is presented to show effective of the present method using a series of experiments.

In future work, the author plans to mount the present three-axis tactile sensors on a micro and robotic fingers to perform verification experiments and will perform edge tracing of an object and object manipulation. In these experiments, the presented recognition method will be effective to determine subtle concave and convex portions located on any surfaces.

5. References

ABAQUS Theory Manual (Ver.5-7), (1998), pp.4.72.1-10.

Amari, T., *Mathematics of Neural Networks*, (1978) , Sangyo-Tosho, (in Japanese).

Borovac, B., Nagy, L., and Sabli, M., Contact Tasks Realization by sensing Contact Forces, *Theory and Practice of Robots and Manipulators* (*Proc. of 11th CISM-IFToNN Symposium*), Springer Wien New York, (1996), pp. 381-388.

Guo, S, Fukuda, T., Kosuge, K., Arai, F., Oguro, K., and Negoro, M., Micro-Catheter Micro System with Active Guide Wire, *Proc. 1995 IEEE Int. Conf. On Robotics and Automation*, (1995), pp. 79-84.

Kawamura, T., Ohka, M., Miyaoka, T., and Mitsuya, Y., Human Tactile Sensation Capability to Discriminate Moving Fine Texture, *Proceedings of IEEE RO-MAN'98* (*IEEE International Workshop on Robot and Human Communication*), (1998), pp. 555-561.

Maekawa, H., Tanie, K., Komoriya, K., Kaneko, M., Horiguchi, C., and Sugawara, T., Development of Finger-shaped Tactile Sensor and Its Evaluation by Active Touch, *Proc. of the 1992 IEEE Int. Conf. on Robotics and Automation*, 1992, pp. 1327-1334.

Maeno, T., Kobayashi, K., and Yamazaki, N., Relationship Between the Structure of Human Finger Tissue and the Location of Tactile Receptors, *Bulletin of JSME International Journal*, Series C, Vol. 41, No. 1, (1998), pp. 94-100.

McCulloch, W. & Pitts, W., A Logical Calculus of the Ideas Imminent in Nervous Activity, *Bulletin of Mathematical Biophysics*, 7 (1943), 115-133.

Mineta, T., Mitsui, T., Watanabe, Y., Kobayashi, S., Haga, Y., and Esashi, M., Batch Fabricated Flat Meandering Shape Memory Alloy Actuator for Active Catheter, *Sensors and Actuators*, A 88, (2001), pp. 112-120.

Miyaoka, T., Module Mechanisms in Tactile Sensation, *Bulletin of Shizuoka Insititute of Science and Technology*, Vol. 3 (1994) , 15-28, (in Japanese)

Moss-Salentijin, L., The Human Tactile System, *Advanced Tactile Sensing for Robotics* (*edited by H. R. Nicholls*), (1992), 123-145.

Mott, D. H., Lee, M. H., and Nicholls, H. R., An Experimental Very High Resolution Tactile Sensor Array, *Proc. 4th Int. Conf. on Robot Vision and Sensory Control*, (1984), pp. 241-250.

Nicholls, H. R., Tactile Sensing Using an Optical Transduction Method, *Traditional and Non-traditional Robot Sensors* (*Edited by T. C. Henderson*), Springer-Verlag, (1990), pp. 83-99.

Nicholls, H. R., *Advanced Tactile Sensing for Robotics* (*H. R. Nicholls, eds.*), World Scientific Publishing, Singapore, (1992), pp. 13-47.

Oka, H. & Irie, T., Bio-mechanical properties for Soft Tissue Modeling, *Biomechanism*, Vol. 17-4 (1993), (in Japanese).

Ohka, M., Kobayashi, M., Shinokura, T., and Sagisawa, S. et al., Tactile Expert System Using a Parallel-fingered Hand Fitted with Three-axis Tactile Sensors, *JSME Int. J., Series C*, Vol. 37, No. 1, 1994, pp. 138-146.

Ohka, M., Mitsuya, Y., Takeuchi, S., Ishihara, H., and Kamekawa, O., A Three-axis Optical Tactile Sensor (FEM Contact Analyses and Sensing Experiments Using a Large-sized Tactile Sensor), *Proc. of the 1995 IEEE Int. Conf. on Robotics and Automation*, 1995, pp. 817-824.

Ohka, M., Mitsuya, Y., Hattori, K., and Higashioka, I., Data Conversion Capability of Optical Tactile Sensor Featuring an Array of Pyramidal Projections, *Proc. of 1996 IEEE/SICE/RSJ Int. Conf. on Multisensor Fusion and Integration for Intelligent Systems*, (1996), pp.573-580.

Ohka, M., Higashioka, I., and Mitsuya, Y., A Micro Optical Three-axis Tactile Sensor (Validation of Sensing Principle Using Models), *Advances in Information Storage Systems*, Vol. 10, (Bhushan, B. & Ono, K., eds.),(World Scientific Publishing, Singapore, 1999), pp. 313-325.

Ohka, M., Mitsuya, Y., Matsunaga, Y., and Takeuchi, S., Sensing Characteristics of an Optical Three-axis Tactile Sensor Under Combined Loading, *Robotica*, (2004), Vol. 22, pp. 213-221.

Ohka, M., Mitsuya, Y., Higashioka, and I., Kabeshita, H., An Experimental Optical Three-axis Tactile Sensor for Micro-Robots, *Robotica*, vol.23-4, (2005), pp. 457-465.

Ohka, M., Kawamura, T., Itahashi, T., Miyaoka, T., and Mitsuya, Y., A Tactile Recognition System Mimicking Human Mechanism for Recognizing Surface Roughness, *JSME International Journal*, Series C, Vol. 48, No.2, (2005), pp.278-285.

Ohka, M., Kobayashi, H., Takata, J., and Mitusya, Y., Sensing Precision of an Optical Three-axis Tactile Sensor for a Robotic Finger, *Proc. of 15th IEEE Int. Proceedings of IEEE RO-MAN'98* (*IEEE International Workshop on Robot and Human Communication*), (2006), (to be published).

Takeuchi, S., Ohka, M., and Mitsuya, Y., Tactile Recognition Using Fuzzy Production Rules and Fuzzy Relations for Processing Image Data from Three-dimensional Tactile Sensors Mounted on a Robot Hand, *Proc. of the Asian Control Conf.*, Vol. 3, 1994, pp. 631-634.

Tanie, K., Komoriya, K., Kaneko, M., Tachi, S., and Fujiwara, A., A High Resolution Tactile Sensor Array, *Robot Sensors Vol. 2: Tactile and Non-Vision, Kempston*, UK: IFS (Pubs), (1986), pp. 189-198.

Vallbo, Å. B. & Johansson, R. S., Properties of Cutaneous Mechanoreceptors in the Human Hand Related to Touch Sensation, *Human Neurobiology*, Vol. 3, (1984), pp. 3-14.

Yoshida, K, Kikuchi, M., Park, J.-H., and Yokota, S., Fabrication of Micro Electro-rheological Valves (ER Valves) by Micromachining and Experiments, *Sensors and Actuators*, A 95, (2002), pp. 227-233.

Mobile Robots: Perception & Navigation

Edited by Sascha Kolski

Today robots navigate autonomously in office environments as well as outdoors. They show their ability to beside mechanical and electronic barriers in building mobile platforms, perceiving the environment and deciding on how to act in a given situation are crucial problems. In this book we focused on these two areas of mobile robotics, Perception and Navigation. This book gives a wide overview over different navigation techniques describing both navigation techniques dealing with local and control aspects of navigation as well es those handling global navigation aspects of a single robot and even for a group of robots.

How to reference

In order to correctly reference this scholarly work, feel free to copy and paste the following:

M. Ohka (2007). Optical Three-Axis Tactile Sensor, Mobile Robots: Perception & Navigation, Sascha Kolski (Ed.), ISBN: 3-86611-283-1, InTech, Available from:
http://www.intechopen.com/books/mobile_robots_perception_navigation/optical_three-axis_tactile_sensor

INTECH
open science | open minds